

# A Comparative Study of Degradation Behaviors of LiFePO<sub>4</sub>, LiMn<sub>2</sub>O<sub>4</sub>, and LiNi<sub>0.8</sub>Mn<sub>0.1</sub>Co<sub>0.1</sub>O<sub>2</sub> in Different Aqueous Electrolytes

To cite this article: Yuxin Zhang et al 2024 J. Electrochem. Soc. 171 020526

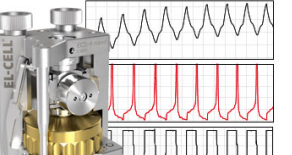
View the article online for updates and enhancements.

#### You may also like

Große et al.

- Modifying Jahn—Teller distortion by epitaxial stress in LaMnO<sub>3</sub> films for tunning electron localization
- Xin Chen, Baohua Wang, Tongxin Ge et al.
- Iron Hexacyanoferrate Based Compound Modified LiMn<sub>2</sub>O<sub>4</sub> Cathodes for Lithium Ion Batteries
- Cheng-Lun Chen, Kuo-Feng Chiu, Hoang Jyh Leu et al.
- La<sub>1</sub>, Mn<sub>4</sub>, O<sub>3</sub>, buffer layers on inclined substrate deposited MgO templates for coated conductors
   Oleksiy Troshyn, Christian Hoffmann, Veit

### Measure the Electrode Expansion in the Nanometer Range. Discover the new ECD-4-nano!





- Capacitive Displacement Sensor (Range 250 µm, Resolution ≤ 5 nm)
- Detect Thickness Changes of the Individual Electrode or the Full Cell.

www.el-cell.com +49 40 79012-734 sales@el-cell.com







## A Comparative Study of Degradation Behaviors of LiFePO<sub>4</sub>, LiMn<sub>2</sub>O<sub>4</sub>, and LiNi<sub>0.8</sub>Mn<sub>0.1</sub>Co<sub>0.1</sub>O<sub>2</sub> in Different Aqueous Electrolytes

Yuxin Zhang, <sup>1</sup> Anyang Hu, <sup>1</sup> Dong Hou, <sup>1</sup> Gihan Kwon, <sup>2</sup> Dawei Xia, <sup>1</sup> Luxi Li, <sup>3</sup> and Feng Lin<sup>1,\*,z</sup>

Aqueous Li-ion batteries (ALIBs) are an important class of battery chemistries owing to the intrinsic non-flammability of aqueous electrolytes. However, water is detrimental to most cathode materials and could result in rapid cell failure. Identifying the degradation mechanisms and evaluating the pros and cons of different cathode materials are crucial to guide the materials selection and maximize their electrochemical performance in ALIBs. In this study, we investigate the stability of LiFePO<sub>4</sub> (LFP), LiMn<sub>2</sub>O<sub>4</sub> (LMO) and LiNi<sub>0.8</sub>Mn<sub>0.1</sub>Co<sub>0.1</sub>O<sub>2</sub> (NMC) cathodes, without protective coating, in three different aqueous electrolytes, i.e., salt-in-water, water-in-salt, and molecular crowding electrolytes. The latter two are the widely reported "water-deficient electrolytes." LFP cycled in the molecular crowding electrolyte exhibits the best cycle life in both symmetric and full cells owing to the stable crystal structure. Mn dissolution and surface reduction accelerate the capacity decay of LMO in water-rich electrolyte. On the other hand, the bulk structural collapse leads to the degradation of NMC cathodes. LMO demonstrates better full-cell performance than NMC in water-deficient aqueous electrolytes. LFP is shown to be more promising than LMO and NMC for long-cycle-life ALIB full cells, especially in the molecular crowding electrolyte. However, none of the aqueous electrolytes studied here provide enough battery performance that can compete with conventional non-aqueous electrolytes. This work reveals the degradation mechanisms of olivine, spinel, and layered cathodes in different aqueous electrolytes and yields insights into improving electrode materials and electrolytes for ALIBs.

© 2024 The Electrochemical Society ("ECS"). Published on behalf of ECS by IOP Publishing Limited. [DOI: 10.1149/1945-7111/ad24c0]

Manuscript submitted November 20, 2023; revised manuscript received December 27, 2023. Published February 14, 2024.

Supplementary material for this article is available online

The exploration of renewable energy and development of energy storage technologies are in great demand, of which Li-ion batteries (LIBs) attract much attention owing to their high energy density. <sup>1-3</sup> However, the intrinsic flammability of organic electrolytes leads to severe safety concerns in conventional LIBs, <sup>4,5</sup> as evidenced by fire accidents of electric vehicles and consumer electronics. Aqueous Li-ion batteries (ALIBs) are regarded as an alternative approach to tackle the safety issue. <sup>6-8</sup> However, the narrow electrochemical stability window (ESW) of water (1.23 V) significantly limits the choice of electrode materials and the output energy densities of ALIBs. Since Dahn's group developed the ALIBs in 1994, <sup>9</sup> significant progress has been made to develop novel aqueous electrolytes with wide ESWs and investigating the electrochemical performance of different electrode materials. <sup>4</sup>

Highly concentrated "water-in-salt" (WIS) electrolyte is one of the most interesting systems in aqueous electrolytes. 10-12 In a WIS electrolyte, most water molecules are expected to participate in the construction of solvation shells and interact with the charged cations or anions through electrostatic force, significantly reducing the reactivity of water molecules and expanding the ESW of aqueous electrolytes. 13-15 Wang's group developed a 21 m lithium bis (trifluoromethanesulfonyl)imide (LiTFSI) aqueous electrolyte, which successfully enlarges the ESW to 2.8 V and realizes stable cycling of a 2.3 V LiMn<sub>2</sub>O<sub>4</sub>/Mo<sub>6</sub>S<sub>8</sub> ASIB over 100 times at low current density (0.15 C). To Since then, various Li salts with high solubility in water have been examined to enrich the library of the WIS electrolytes, including but not limited to LiCl, <sup>16</sup> and LiNO<sub>3</sub>. <sup>1</sup> Follow-up studies showed that bi-salt WIS electrolytes can further expand the ESW to 3.1 V,7 approaching those of commercial nonaqueous electrolytes. However, the high cost associated with excessive salts has impeded the large-scale applications of WIS electrolytes. 12

\*Electrochemical Society Member.

zE-mail: fenglin@vt.edu

Molecular-crowding (MC) electrolyte is another family of aqueous electrolytes, although they can contain substantial amounts of organic molecules. MC electrolytes usually have less amounts of salts. The co-solvent including water and molecular-crowding agents (macromolecules) is used in MC electrolytes, where the water solvation environment is regulated by MC agents through the construction of a strong hydrogen bonding network. Confining water in a polyethylene glycol (PEG) agent has been shown to be capable of suppressing the hydrogen evolution reaction and enlarging the ESW to 3.2 V. The modification of functional groups of MC agents can further tune the viscosity of MC aqueous electrolytes and modulate the rate capability of batteries where MC electrolytes are used. On the same suppression of the same suppre

Although both electrolyte systems show potential for applications, a comprehensive study is needed to demonstrate how different cathodes behave in these electrolytes, including the electrochemical performance, surface and bulk structural changes of cathode materials, and transition metal (TM) dissolution, which can serve as a reference to identify the most compatible cathode-electrolyte system and inform the advantages and disadvantages of different electrolytes. Herein, we select LiFePO<sub>4</sub> (LFP), LiMn<sub>2</sub>O<sub>4</sub> (LMO), and LiNi<sub>0.8</sub>Mn<sub>0.1</sub>Co<sub>0.1</sub>O<sub>2</sub> (NMC) as the model materials to represent the most classical olivine, spinel, and layered crystal structures and to directly compare their behaviors in aqueous electrolytes. For the aqueous electrolytes, we prepare 2 M lithium LiTFSI electrolyte ("salt-in-water," SIW), 21 m LiTFSI electrolyte (WIS), and 2 M LiTFSI-94% polyethylene glycol (PEG400)–6%H<sub>2</sub>O electrolyte (MC) for our cross-comparison experiments. The results show that LFP is the most stable cathode in all electrolytes with minor Fe dissolution and negligible structural change, but the output energy density is the bottleneck owing to the low average discharge potential. Both LMO and NMC cathodes show more inferior cycle life than LFP materials. Mn dissolution and surface reconstruction are the dominant degradation mechanisms in LMO cathodes, whereas the water-induced bulk structural collapse leads to rapid failure of NMC materials in water rich electrolyte. Reducing the water content in aqueous electrolytes can notably improve the

<sup>&</sup>lt;sup>1</sup>Department of Chemistry, Virginia Tech, Blacksburg, Virginia 24061, United States of America

<sup>&</sup>lt;sup>2</sup>National Synchrotron Light Source II, Brookhaven National Laboratory, Upton, New York 11973, United States of America

<sup>&</sup>lt;sup>3</sup>Advanced Photon Source, Argonne National Laboratory, Lemont, Illinois 60439, United States of America

performance of LMO full cells. Nevertheless, more efforts are desired to elevate the energy density and lower the cost to accelerate its practical applications.

#### **Experimental**

*Materials preparation.*—LiFePO $_4$  (LFP), LiMn $_2$ O $_4$  (LMO), LiNi $_0.8$ Mn $_0.1$ Co $_0.1$ 0 $_2$  (NMC), Li $_4$ Ti $_5$ O $_{12}$  (LTO) were provided by the U.S. Department of Energy's (DOE) CAMP Facility (Cell Analysis, Modeling and Prototyping) at Argonne National Laboratory. 3,4,9,10-perylenetetracarboxylic diimide (PTCDI) was purchased from Alfa Aesar (CAS 81-33-4). The Lithium bis(trifluoromethanesulfonyl) imide (LiTFSI) salt (99.95%) and Polyethylene glycol (PEG 400) solution were purchased from Sigma Aldrich.

Electrochemical measurements.—LFP, LMO and NMC slurries were prepared by mixing active materials, carbon black and polyvinylidene fluoride (PVDF) with a weight ratio of 8:1:1 and then casted on the carbon-coated aluminum foil. The mass loading was estimated to be  $\sim$ 3.5, 4 and 6 mg cm<sup>-2</sup>, respectively. The 2 mol  $1^{-1}$ lithium bis(trifluoromethanesulfonyl)imide (LiTFSI) and 21 mol kg<sup>-1</sup> aqueous electrolytes were prepared by dissolving stoichiometric amount of LiTFSI in DI water. The 2 M LiTFSI-94%PEG-6%H<sub>2</sub>O electrolyte was prepared by mixing the PEG400 with water and dissolving the designated amount of LiTFSI in the mixed solvents. To assemble the symmetric cell, different cathodes were assembled with the Li<sub>4</sub>Ti<sub>5</sub>O<sub>12</sub> (LTO) anode using the MC electrolyte and charged to obtain the pre-delithiated cathodes. 100%, 70% and 50% Li-ions were extracted from LFP, LMO and NMC electrodes, respectively, to prepare the pre-delithiated cathode materials. The calculation is based on coulometry. Then the pre-delithiated cathodes and pristine cathodes were used to assemble the symmetric cells. The applied current density of the pre-delithiation process and symmetric cell cycling was 10 mA g<sup>-1</sup> based on the active cathode mass. The full cells were made by using different pristine cathodes and PTCDI anodes, and the current density was 20 mA g<sup>-1</sup>. To access the maximum capacity and minimize the side reactions happening in different full cells, the voltage ranges were determined to be 0-1.9 V (LFP||PTCDI cell in the WIS electrolyte), 0-2.0 V (LFP||PTCDI cell

in the MC electrolyte), 0.4– $2.3\,V$  (LMOIIPTCDI cell in the WIS electrolyte), 0– $2.5\,V$  (LMOIIPTCDI cell in the MC electrolyte), and 0– $2.6\,V$  (NMCIIPTCDI cell in the MC electrolyte).

Materials characterizations.—Scanning electron microscopy (SEM) was conducted on a LEO 1550 field-emission instrument with an accelerating voltage of 6 kV. Lab X-ray diffraction (XRD) results were obtained on a Rigaku Miniflex II diffractometer with a Cu K $\alpha$  X-ray radiation ( $\lambda = 1.54 \,\text{Å}$ ) in a scan range of  $10^{\circ}$ – $60^{\circ}$ . Synchrotron XRD patterns were collected at beamline 28-ID-1 at NSLS-II with a wavelength of 0.1665 Å. The electrode samples were sealed in between Kapton tapes, and patterns were recorded with a collection time of 20 s. Ni was used for calibration. The obtained 2D patterns were then integrated into 1D patterns using the DIOPTAS software. The XRD patterns were converted to the Cu K $\alpha$ -based XRD with the wavelength of 1.5406 Å. X-ray fluorescence microscopy (XFM) measurements were conducted at the 8-BM-B beamline at the Advanced Photon Source, Argonne National Laboratory. The samples were raster-scanned by a sub-micrometer focused 10 keV X-ray beam with a step size of 25  $\mu$ m. The fluorescent Xrays were detected with a four-element silicon-drift Vortex detector and the raw data were processed and quantified with MAPS. The cells after different cycle numbers were disassembled and the separators were used for XFM measurements. X-ray photoelectron spectroscopy (XPS) measurements were performed on a PHI VersaProbe III with a monochromatic Al K-alpha X-ray source (1486.6 eV). Ar sputtering was applied to the samples at a sputtering rate of 0.9 nm min<sup>-1</sup>. The emission angle is 45 degrees and the pass energy for different elements is 26 eV. The synchrotron XRD and XFM samples were sealed in between Kapton tapes and stored in a Ar-filled glove box before measurements. The XPS samples were attached to the sample holder in the glovebox prior to being transferred to the measurements.

#### **Results and Discussion**

Morphology stability of different cathodes in the electrolytes.— The soaking experiments are first conducted to evaluate the intrinsic stability of cathode materials in various electrolytes (Fig. 1). LFP

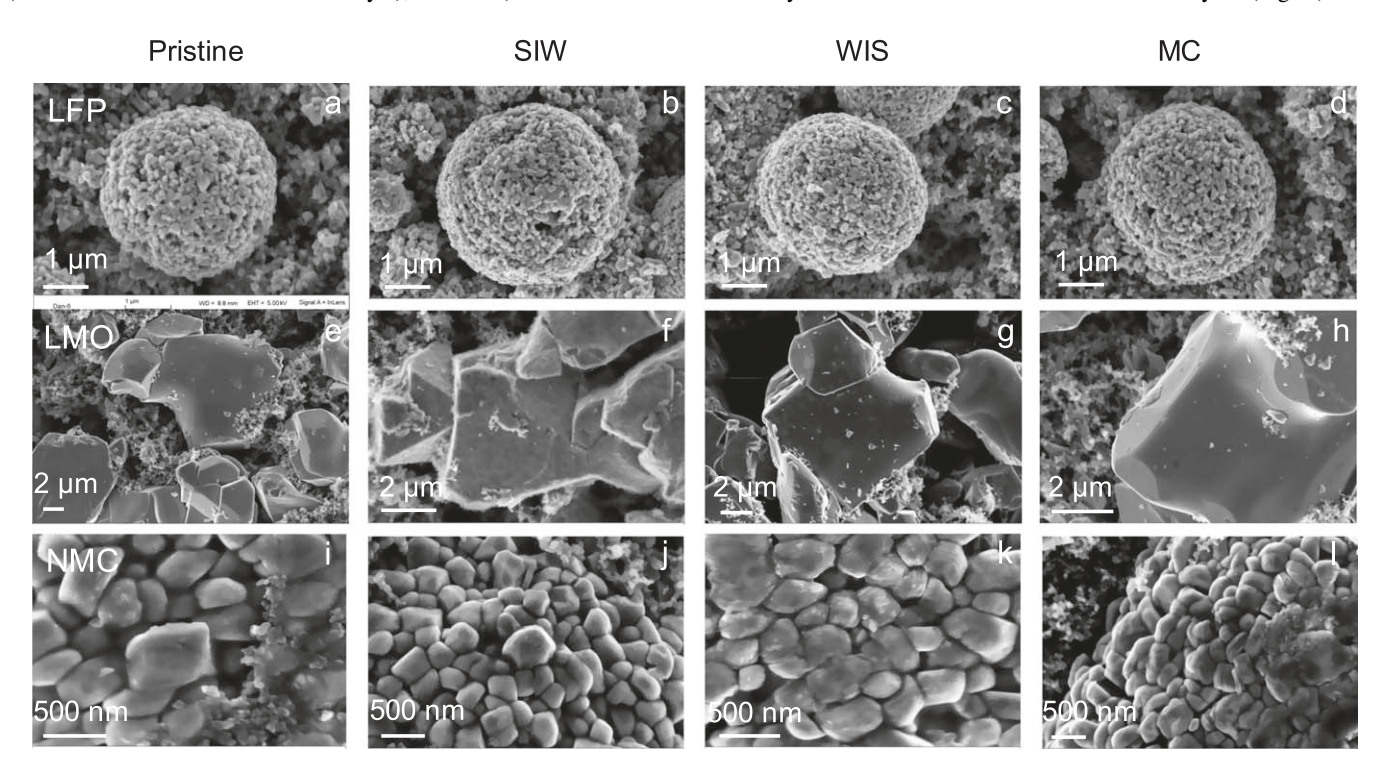


Figure 1. The surface morphology of particles in (a)—(d) LFP, (e)—(h) LMO and (i)—(l) NMC cathodes at the pristine state and after soaking in different electrolytes for three days. The electrodes were rinsed with dimethoxyethane (DME) and dried in a vacuum oven prior to SEM imaging.

shows great storage stability in different electrolytes without significant morphology change (Figs. 1a–1d). Although LMO remains stable in WIS and MC electrolytes (Figs. 1g–1h), it suffers severe morphology change in the SIW electrolyte (Fig. 1f), where the particle surface becomes fluffy. On the other hand, NMC exhibits some degree of exfoliation on the surface, especially in the WIS electrolyte (Fig. 1k), which is likely associated with metal dissolution and hydration of the particle surface. The results suggest that LMO and NMC are more susceptible to water damage. Noted that there could be nanoscale changes that go beyond the detection limit of SEM and can influence battery performance.

Electrochemical performance of different cathodes in symmetric cells.—To analyze the cathode performance and exclude the potential effect of the anode, the symmetric-cell configuration is adopted for the electrochemical measurements. The pre-delithiated cathodes are collected from full cells after the charging process (Fig. S1) and are then paired with pristine cathodes to assemble symmetric cells. Based on the coulometry, 100% and 70% Li ions are extracted from LFP and LMO. To avoid the potential side reactions at high voltage, the NMC cathode is partially charged to 50% Li-ion extraction. The high water content in SIW electrolytes causes water co-intercalation and poor Li<sup>+</sup> intercalation/deintercalation efficiency, leading to rapid failure of all cells (Fig. S2). LFP shows reasonably good capacity retention and coulombic efficiency (~99.6%) in the WIS and MC electrolytes (Figs. 2a–2b, 3a–3b), of which MC electrolyte enables a higher specific capacity.

LMO and NMC demonstrate a similar degree of rapid capacity degradation in the WIS and MC electrolytes (Figs. 2c–2f, 3c–3f) with a compromised coulombic efficiency (~99.0%). Considering that NMC exhibits more severe morphological change than LMO in the soaking experiments (Fig. 1), one would think that NMC would be less stable than LMO. However, Figs. 2 and 3 show these two materials have similar fading behaviors. Therefore, there are other factors beyond the surface morphological changes that influence cycling stability. We then performed more extensive investigations into the degradation mechanisms.

*Transition metal dissolution behaviors.*—Transition metal (TM) dissolution is analyzed by using X-ray fluorescence microscopy (XFM), which can provide quantitative information and spatial distribution of dissolved species. <sup>21–23</sup> After the initial three cycles, the symmetric cells are disassembled, and the separators are used for measurements and quantitative analysis of dissolved species.

As shown in Figs. 4a–4c, the Fe dissolution from LFP is negligible in all the electrolytes, confirming the excellent TM stability of LFP in the presence of water. In contrast, LMO shows severe Mn dissolution during cycling, especially in the SIW electrolyte. The redox-active Mn<sup>3+</sup> is subject to the Jahn-Teller distortion and prone to experience disproportion reactions, where the generated Mn<sup>2+</sup> can be easily dissolved into the electrolyte. Moreover, the MC electrolyte induces a slightly higher amount of Mn dissolution than the WIS electrolyte for the LMO electrode (Table I), which could originate from a higher content of Mn<sup>3+</sup> on the surface after cycling in MC electrolytes and will be discussed in the later section.

Although the Ni and Mn dissolution has been detected in NMC materials (Figs. 4g–4i, S3), the total quantity of dissolved species is lower than LMO (Table I). The dissolved Ni/Mn mass ratio is calculated to be  $\sim$ 15.3 in the SIW electrolyte, corresponding to an atomic ratio of  $\sim$ 14.3. Given that the Ni/Mn atomic ratio in pristine NMC is 8, Ni dissolution is more severe than Mn dissolution when NMC811 is cycled in the SIW electrolyte. The ratio is reduced to  $\sim$ 2.1 in the WIS electrolyte and  $\sim$ 2.2 in the MC electrolyte. Since the detected Mn concentration is at a similar level in all the electrolytes, the Ni dissolution is significantly inhibited when the content of free water molecules is lowered in aqueous electrolytes. We can also observe that the TM prefers to deposit at the near-edge position over the center region, which could be associated with the heterogeneous current or pressure distribution. 25

The differences in the dissolution behavior become more pronounced after extended cycles (Fig. 5) for LMO, including more severe TM dissolution and edge-region accumulation. The total amount of dissolved Mn reaches  $\sim 10.8 \ \mu g \ cm^{-2}$  in the WIS electrolyte and  $\sim 20.1 \ \mu g \ cm^{-2}$  in the MC electrolyte (Table II). In

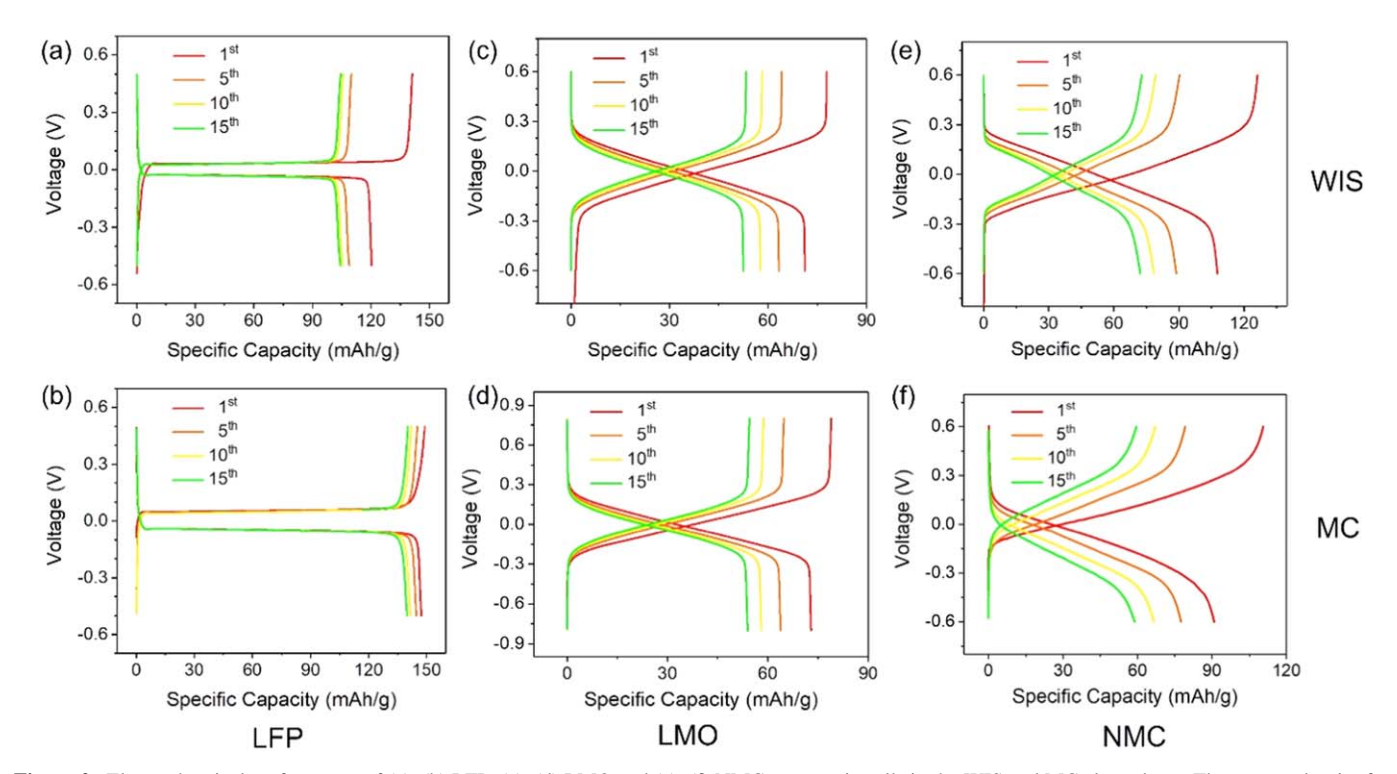


Figure 2. Electrochemical performance of (a)–(b) LFP, (c)–(d) LMO and (e)–(f) NMC symmetric cells in the WIS and MC electrolytes. The current density for all cells is 10 mA  $g^{-1}$ . The current density and specific capacity are calculated based on the mass of active materials in fully lithiated electrodes.

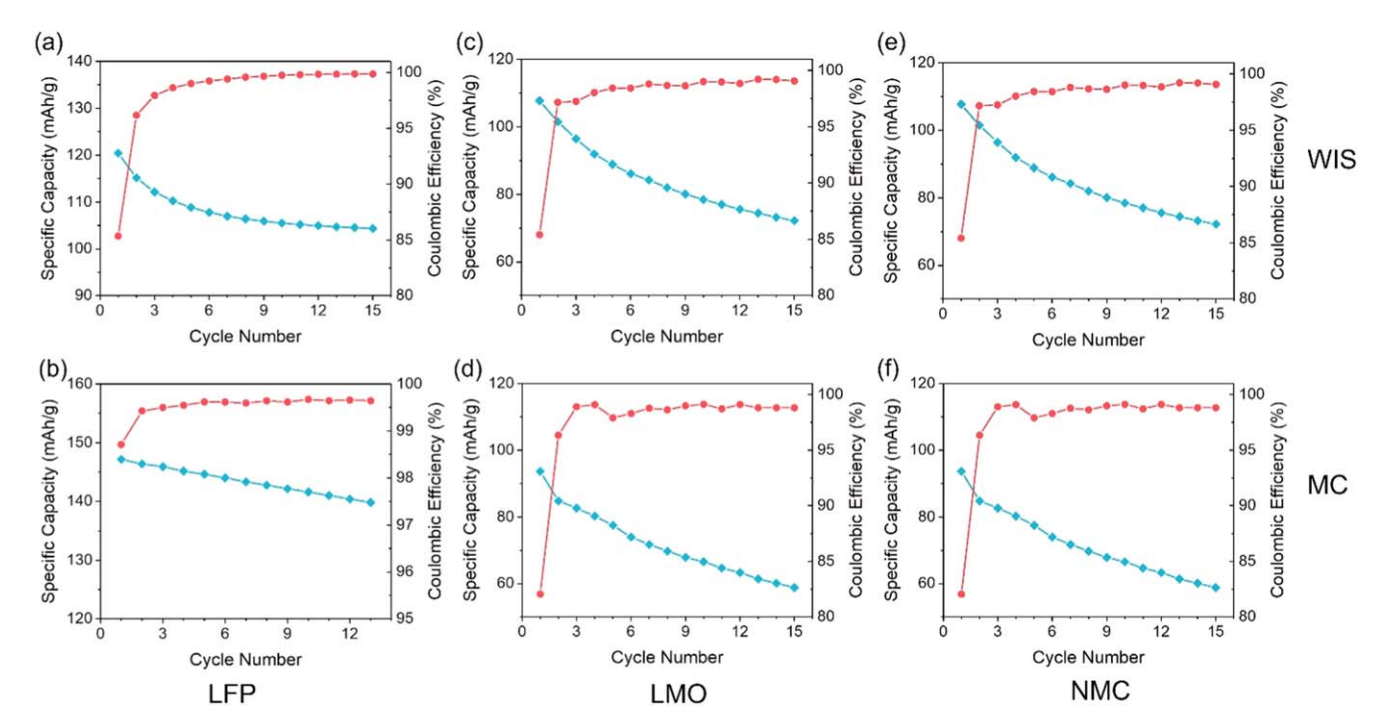


Figure 3. The coulombic efficiency (red) and discharge capacity (cyan) of (a)–(b) LFP, (c)–(d) LMO and (e)–(f) NMC symmetric cells cycled in the WIS and MC electrolytes within the first 15 cycles. The LFP symmetric cells exhibit the best capacity retention and the highest average coulombic efficiency of  $\sim$ 99.8% compared to LMO and NMC.

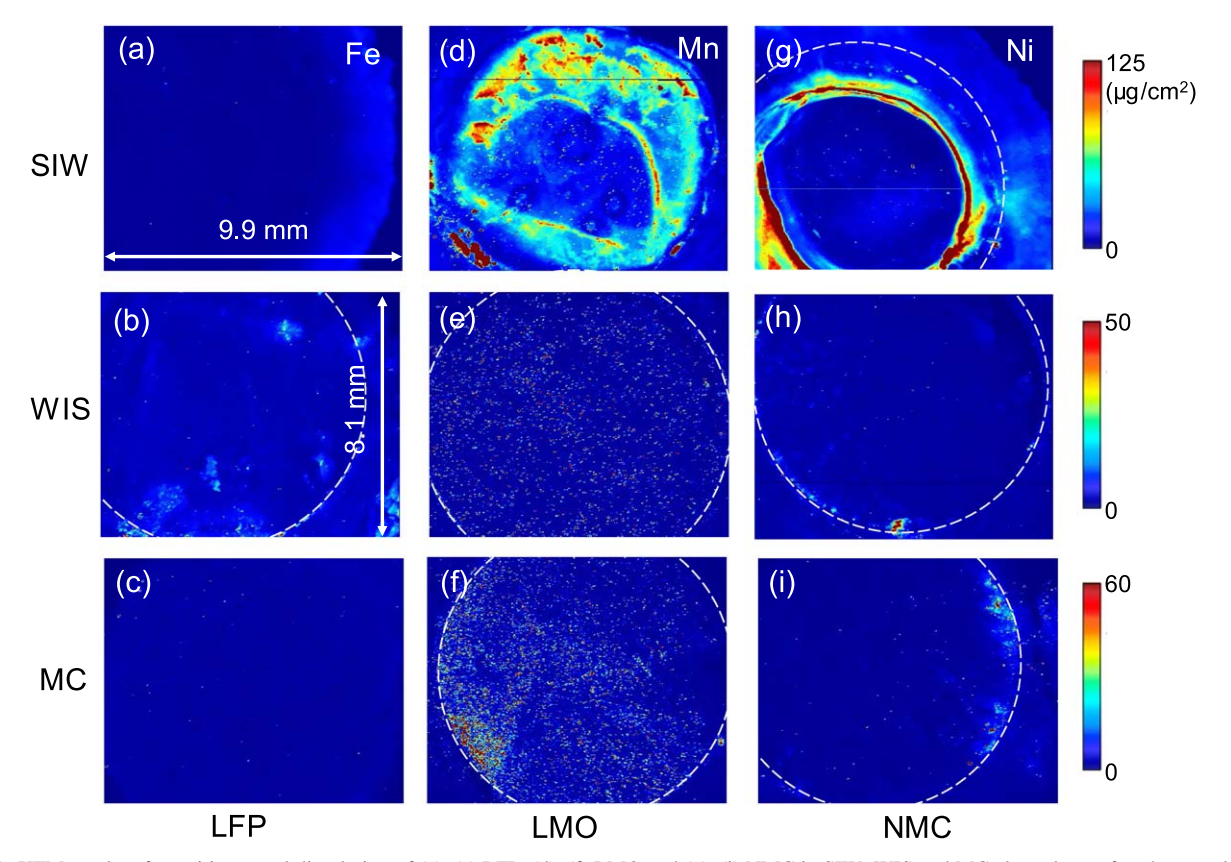


Figure 4. XFM results of transition metal dissolution of (a)–(c) LFP, (d)–(f) LMO and (g)–(i) NMC in SIW, WIS and MC electrolytes after three cycles in the symmetric cell configuration. The current density for all symmetric cells is  $10 \text{ mA g}^{-1}$ . After cycling, the cells are disassembled, and the separators are used for the measurements. The white dash curves denote the edges of the electrodes.

Table I. Quantitative TM dissolution of different cathodes in aqueous electrolytes after three cycles in the symmetric cell configuration. cells are disassembled after cycling, and separators are collected for the XFM measurements.

	SIW electrolyte $(\mu g/\text{cm}^2)$	WIS electrolyte $(\mu g/cm^2)$	MC electrolyte (µg/cm²)
LiFePO <sub>4</sub> (Fe)	0.4	3.1	1.6
$LiMn_2O_4(Mn)$	25.3	3	4.9
$LiNi_{0.8}Mn_{0.1}Co_{0.1}O_{2}(Ni)$	19.1	1.7	1.8
$LiNi_{0.8}Mn_{0.1}Co_{0.1}O_2(Mn) \\$	1.3	0.8	0.8

Table II. Quantitative TM dissolution of different cathodes after long-term cycling (50 cycles for LFP, 100 cycles for LMO and NMC) in WIS and MC electrolytes.

	WIS electrolyte $(\mu g/cm^2)$	MC electrolyte (µg/cm²)
LiFePO <sub>4</sub> (Fe)	3.6	2.7
$LiMn_2O_4(Mn)$	10.8	20.1
$LiNi_{0.8}Mn_{0.1}Co_{0.1}O_2(Ni)$	3.6	3.3
$LiNi_{0.8}Mn_{0.1}Co_{0.1}O_2(Mn)$	1.8	1.3

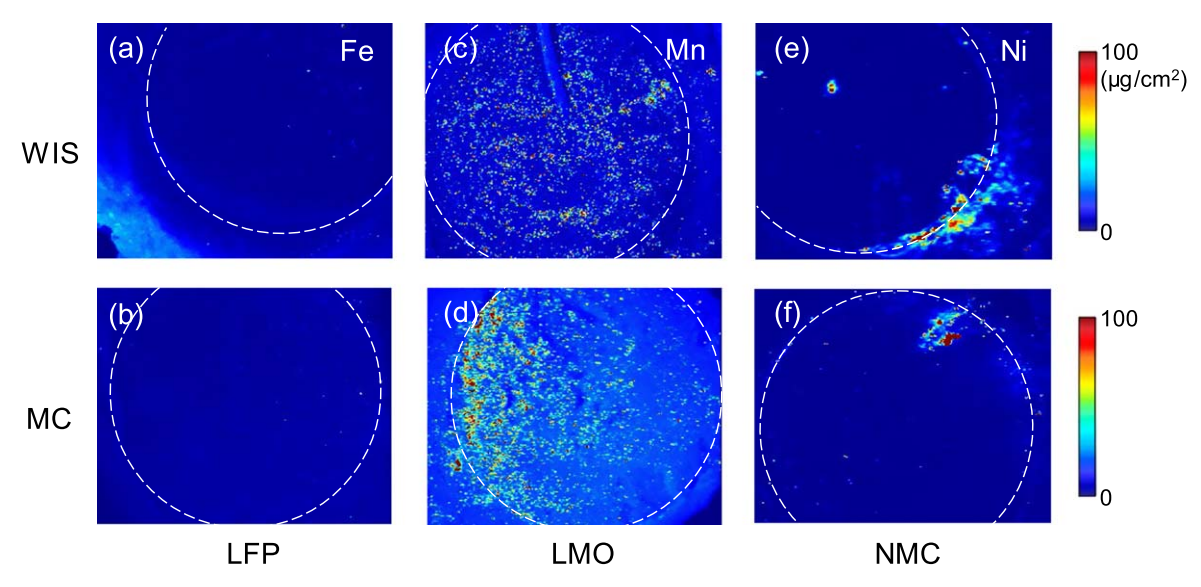


Figure 5. XFM results of transition metal dissolution of (a)–(b) LFP, (c)–(d) LMO and (e)–(f) NMC in the WIS and MC electrolytes after extended cycling in the symmetric cell configuration (50 cycles for LFP and 100 cycles for LMO and NMC). The separators in cycled cells are used for the measurements. The white dash curves indicate the edges of the electrodes.

contrast, the dissolved TMs only slightly increase for LFP and NMC in both electrolytes. Therefore, although the morphology stability of LMO is better than layered NMC materials, TM dissolution likely plays a more important role in battery performance decay.

Electrode surface properties.—Surface changes such as the formation of cathode-electrolyte interphase (CEI) and surface reconstruction during the cycling also influence the degradation and coulombic efficiency of the materials. Herein we select LMO as an example for the investigation. The surface chemical environments after cycling are measured by X-ray photoelectron spectroscopy (XPS). The SIW electrolyte is excluded from the measurements since the cells undergo immediate failure during cycling. At the pristine state, we can notice the existence of Li<sub>2</sub>CO<sub>3</sub> on the surface based on the C 1 s and O 1 s spectra (Fig. 6), <sup>26</sup> which originates from the side reaction between LMO, ambient CO<sub>2</sub> and moisture. <sup>22</sup> The single peak in the F 1 s spectrum is assigned to the CH<sub>2</sub>-CF<sub>2</sub> in the

PVDF binder.<sup>26</sup> After cycling in the WIS and MC electrolytes, the peak position and shape barely change in C 1 s, O 1 s and F 1 s spectra, suggesting no obvious CEI formation on the cycled electrode surface. Although previous studies have reported the appearance of inorganic (LiF, Li<sub>2</sub>CO<sub>3</sub>) and organic species derived from TFSI decomposition on the cathode surface after cycling in these aqueous electrolytes,<sup>27</sup> we do not observe this phenomenon in our study. The reason could be that a longer time of cycling (>20 cycles) is necessary for the CEI formation in aqueous batteries.

Furthermore, the fact that no additional peak appears in the XPS depth profiling of the LMO and LFP electrodes cycled in MC electrolytes (Figs. 7, S4) confirms that the CEI is not formed. The gradually increased LiF content in the F 1 s spectra from the surface to sub-surface in all the cycled electrodes could originate from the PVDF decomposition under Ar<sup>+</sup> sputtering. <sup>28–30</sup>

In the Mn 2p spectra, we can observe that the binding energy slightly shifts to a lower value and the Mn<sup>3+</sup> content increases in the

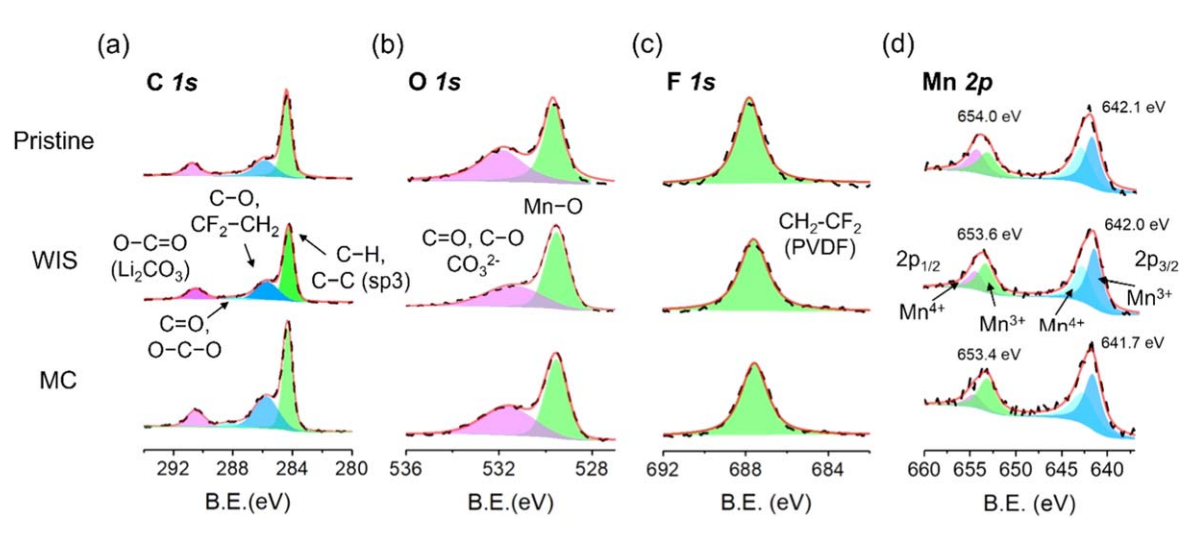


Figure 6. XPS results of (a) C 1 s, (b) O 1 s, (c) F 1 s, and (d) Mn 2p spectra of the pristine and cycled LMO electrodes in the WIS and MC electrolytes, where the black dash curves are the experimental data, and the red solid lines are the fitted data. The electrodes are collected after 2.5 cycles.

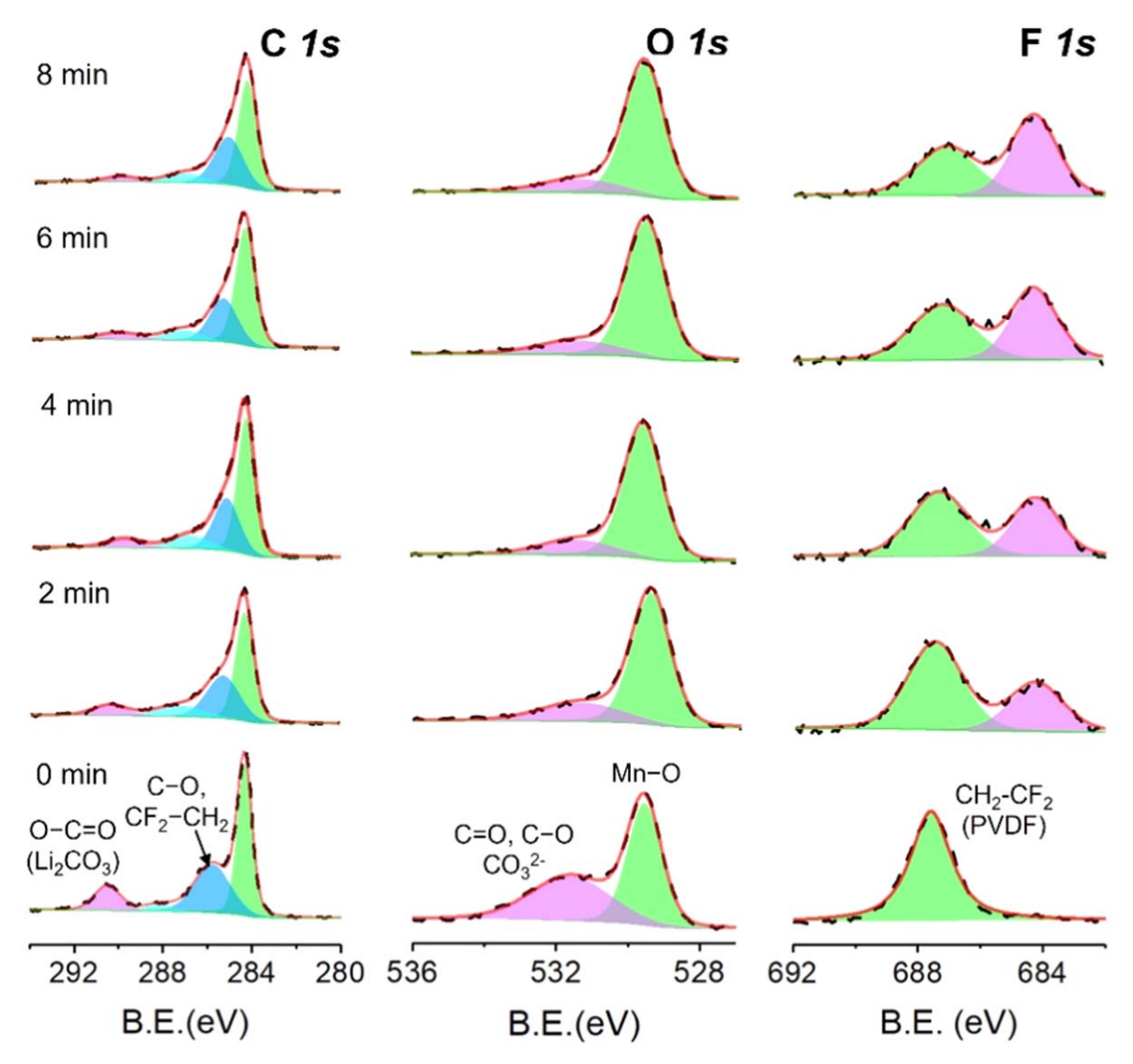


Figure 7. XPS depth profiling of the cycled LMO cathode in the MC electrolyte, where the black dash curves are the experimental data, and the red solid lines are the fitted data. The electrodes are collected after 2.5 cycles.

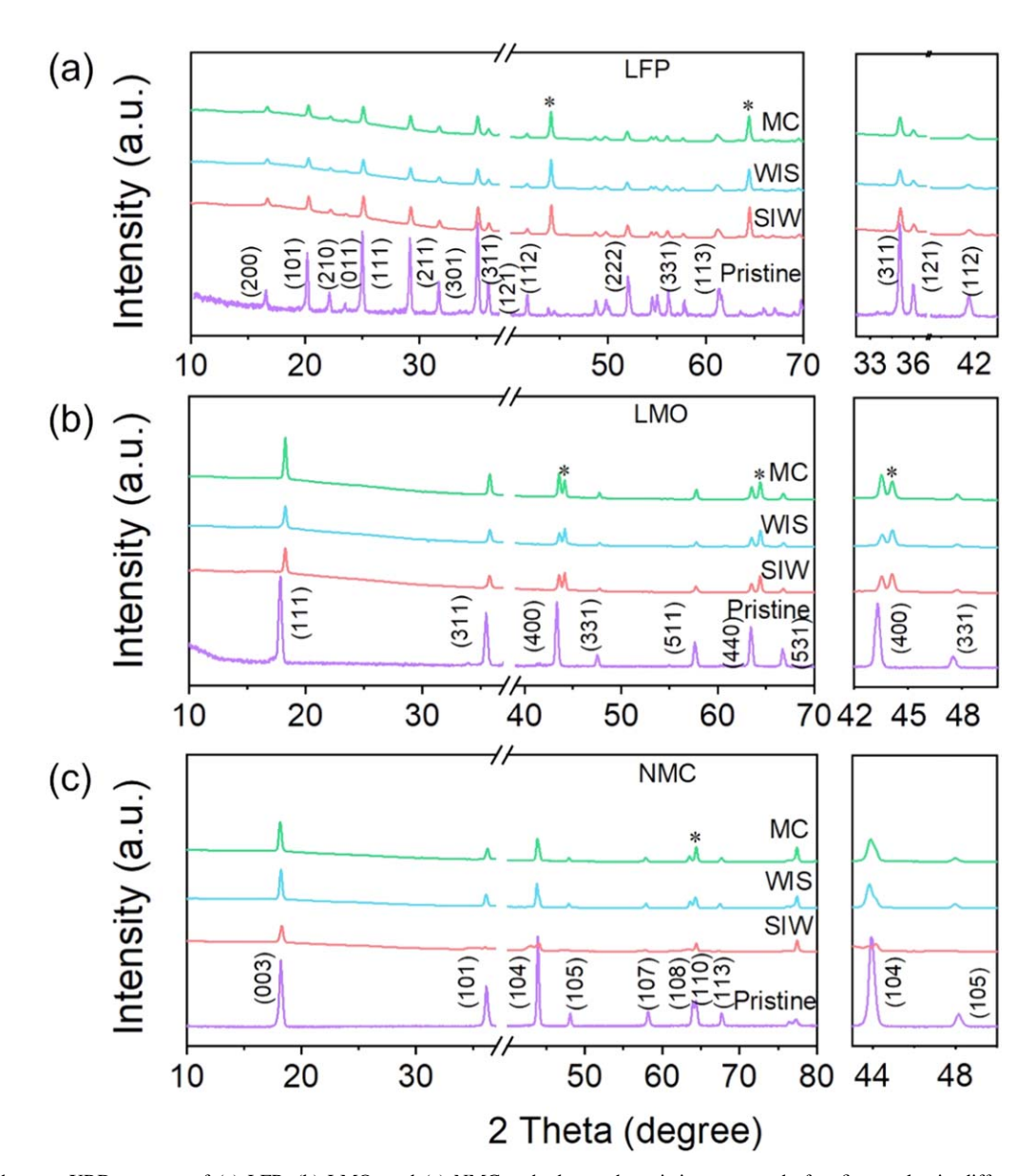
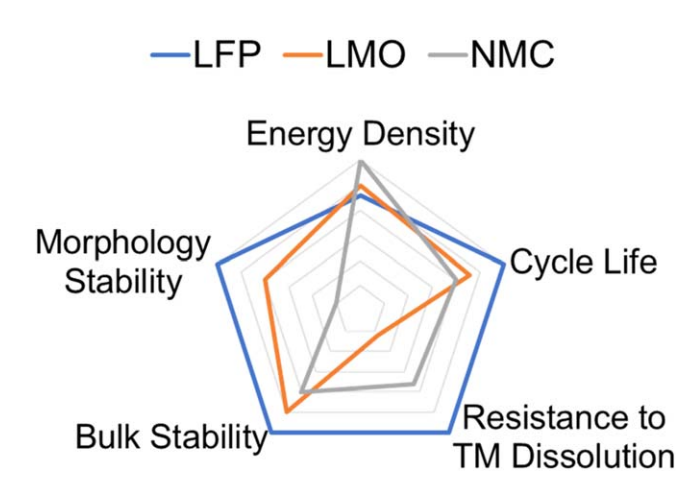


Figure 8. Synchrotron XRD patterns of (a) LFP, (b) LMO, and (c) NMC cathodes at the pristine state and after five cycles in different electrolytes. The corresponding zoom-in regions of the patterns are shown to the right. The peaks labeled by the asteroid symbol belong to the Al foil current collector.

cycled electrodes (Fig. 6), indicating a reduced surface layer,  $^{31}$  agreeing with previous reports and stemming from the potential formation of  $\rm Mn_3O_4.^{24,32}$  Since  $\rm Mn^{3+}$  suffers from severe Jahn-Teller distortion and is prone to dissolve into the electrolyte, the higher  $\rm Mn^{3+}$  content of the LMO electrode cycled in the MC electrolyte is expected to trigger more severe Mn dissolution than that cycled in the WIS electrolyte, which is in line with our XFM results (Tables I and II).

Noted that TM dissolution also impacts the interphase formation during cycling. Compared to non-aqueous batteries, the Jahn-Teller active species Mn<sup>3+</sup> and Ni<sup>3+</sup> undergo more severe dissolution due to the presence of a higher proton concentration in aqueous electrolytes.<sup>33</sup> The dissolved TM ions can accumulate near the cathode surface and generate a diffusion layer,<sup>34</sup> impacting the interphase formation on cathode surface.

**Bulk structural stability.**—Finally, we examine the bulk structural changes of all the materials using synchrotron X-ray diffraction (XRD). The electrodes are collected after five complete cycles. Figure 8a shows that the lattice structure of LFP is well-preserved in all the electrolytes and highlights the superiority of the olivine phase in aqueous systems.



**Figure 9.** Radar plot of the key factors that determine the performance of LFP, LMO and NMC in the aqueous electrolytes. The cycle life is evaluated based on the performance of symmetric cells. The data points located in outer pentagon indicates higher ratings.

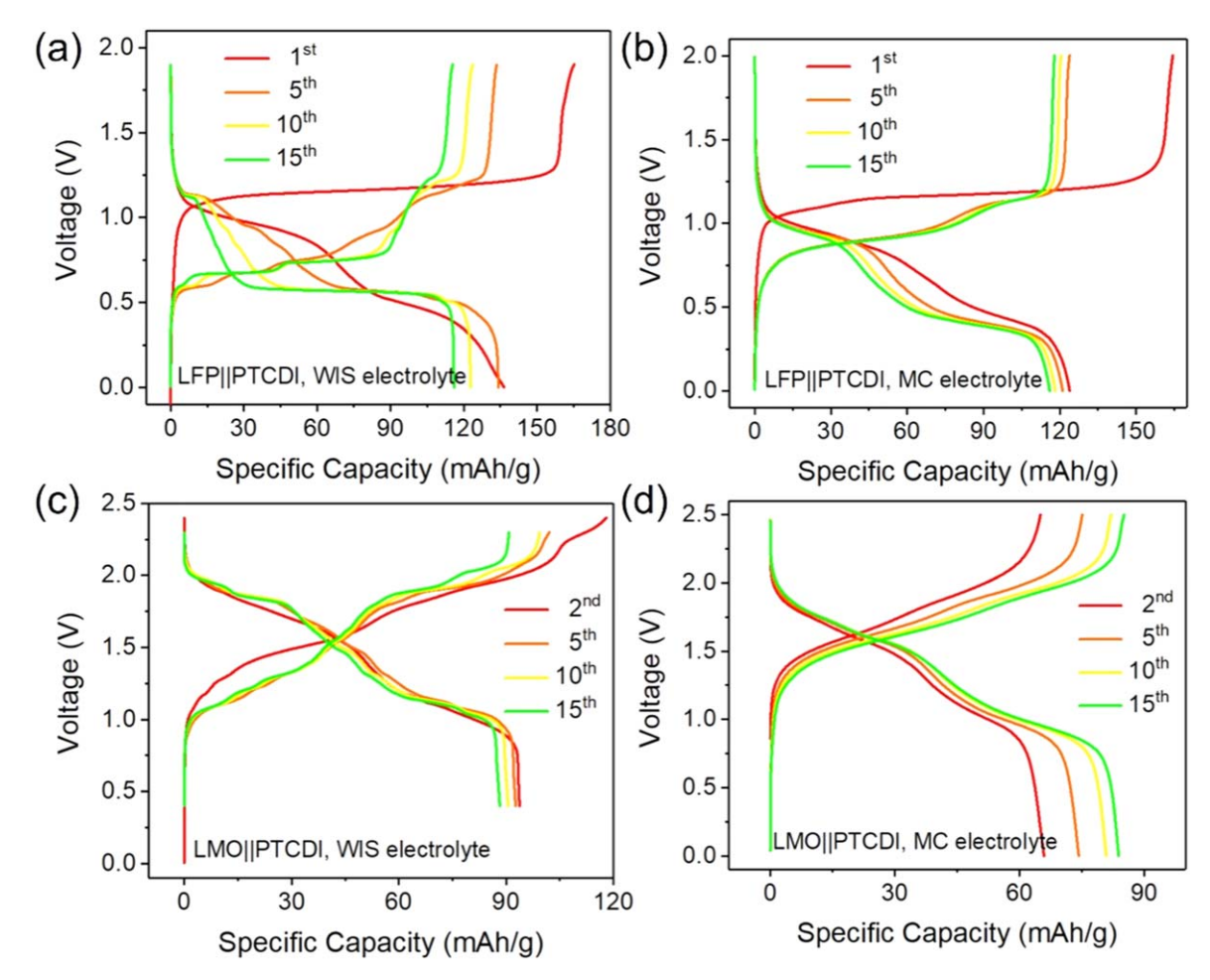
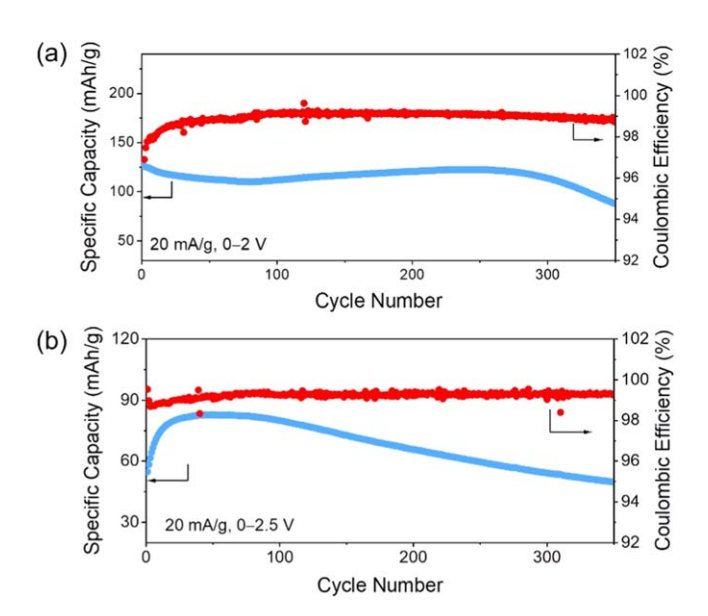


Figure 10. The electrochemical performance of (a) LFP||PTCDI full cell in the WIS electrolyte, (b) LFP||PTCDI full cell in the MC electrolyte, (c) LMO||PTCDI full cell in the WIS electrolyte, (d) LMO||PTCDI full cell in the MC electrolyte. The voltage ranges of different cells are 0-1.9 V, 0-2.0 V, 0.4-2.3 V and 0-2.5 V, respectively. The current density for all cells is  $20 \text{ mA g}^{-1}$ . The upper cutoff voltage of LMO||PTCDI full cell is larger due to a higher average redox potential of  $\text{Mn}^{3+}/\text{Mn}^{4+}$ . The current density and specific capacity are calculated based on the mass loading of active cathode materials.



**Figure 11.** Long-term cycling performance of (a) LFPIIPTCDI and (b) LMOIIPTCDI full cells in the MC electrolyte. The current density is calculated based on the mass loading of active cathode materials. The voltage ranges are varied in order to maximize the cyclable capacity of LFP and LMO materials.

Although the spinel phase can be observed in the LMO electrode after cycling, the zoom-in region (Fig. 8b) shows that the peak intensity is diminished, especially in the SIW and WIS electrolytes, implying that the crystallinity is decreased in the presence of water.

Some characteristic peaks of NMC disappear, and the layered lattice structure collapses after cycling in the SIW electrolyte (Fig. 8c). Considering the previous reports have shown that Nirich NMC materials experience negligible bulk structural change after soaking in the water for one week, 35 we believe the electrochemical reactions during cycling (e.g., water co-intercalation) significantly interrupt the chemical environment in the lattice and degrade the entire structure. In contrast, although the surface exfoliation of NMC is observed (Figs. 1k and 1l) in the WIS and MC electrolytes, the layered structure is well maintained after cycling in these two electrolytes owing to the reduced content and activity of free water molecules.

To conclude, LFP shows the best structural compatibility with all of the aqueous electrolytes studied here, whereas LMO and NMC preserve the basic structural integrity in the WIS and MC electrolytes.

Evaluation of different cathodes.—Combining the above results, we evaluate the performance of different cathode materials from five aspects and summarize the results in Fig. 9. When high energy density is not strictly required in the application, LFP is the best choice owing to its excellent chemical and electrochemical stability against water. In comparison, LMO provides a comparable energy

density with LFP but shows slightly reduced crystallinity and apparent Mn dissolution in these aqueous electrolytes. Given the higher working voltage and acceptable cycle life, LMO can be applied to high-voltage ALIBs to experimentally examine the enlarged ESW of novel aqueous electrolytes. The layered oxides exhibit the worst cycle life and morphology integrity in these electrolytes, which calls for proper electrode modification and electrolyte design.

Full-cell performance.—To gain more insights into the impact of different aqueous electrolytes, we test the full cell performance using 3,4,9,10-perylenetetracarboxylic diimide (PTCDI) as the anode. Compared to the WIS electrolytes (Figs. 10a, 10c and S5), the MC electrolyte allows the LFP and LMO full cells to exhibit better cycle life (Figs. 10b and 11). The initial capacity of LFPII PTCDI cells in the MC electrolyte can reach up to 127 mAh g with a 69.4% retention after 350 cycles (Fig. 11a). In comparison, LMO||PTCDI cells in the MC electrolyte show lower initial specific capacity (Fig. 10d) and worse capacity retention (60.4% after 350 cycles, Fig. 11b). Both cathodes realize over 99% average coulombic efficiency in full cell configuration. On the other hand, the NMC||PTCDI full cell presents an inferior capacity and initial coulombic efficiency during cycling (Fig. S6), indicating the incompatibility of NMC cathodes and aqueous electrolytes.

Overall, the MC electrolyte enables better electrochemical performance than the WIS electrolyte under conditions applied in this study. A better electrochemical performance and higher coulombic efficiency can be achieved through effective bulk doping and surface coating of cathode materials to enhance the structural stability and mitigate the TM dissolution caused by the Jahn-Teller distortion. Additionally, particle size engineering is another feasible approach to inhibit interfacial side reactions.

#### Conclusions

Aqueous batteries attract intensive attention recently owing to the non-flammable nature of the electrolytes. However, the intrinsic narrow electrochemical ESW of water (1.23 V) significantly limits the choice of electrode materials and the output energy density. Moreover, some cathode materials are incompatible with water, imposing great challenges to the large-scale application of aqueous batteries. Many efforts have been devoted to designing aqueous electrolytes to reduce the content of free water molecules and expand the ESW. The WIS and MC electrolyte represent two of the major categories of aqueous electrolytes with over 3.0 V ESWs. Nevertheless, there is a lack of systematic study regarding how commercialized cathode materials behave in different aqueous electrolytes. Such a study would inform future electrode and electrolyte modifications.

Herein, we select three electrolytes with different water contents (SIW, WIS and MC) as the platform to investigate the performance and degradation mechanisms of LFP, LMO and NMC. Combining the electrochemical measurements with XFM, XRD and XPS analyses, we show that LFP exhibits negligible Fe dissolution and morphological/structural degradation during cycling, leading to the best cycle life in both symmetric and full cells. LMO delivers comparable initial energy density in full cell but undergoes the most severe Mn dissolution and surface reduction. Since LMO has higher average redox potentials than LFP and performs well in waterdeficient aqueous environment, it is a good platform material to study the novel aqueous electrolytes with significantly expanded ESWs. The morphological and structural degradation are the biggest concerns for the application of layered oxide materials (e.g., NMC811) in aqueous batteries. Overall, depending on the application areas, LFP and LMO are currently more promising than layered oxides for ALIBs, especially in the MC electrolyte. Nevertheless, there are other factors that can potentially influence the conclusion obtained here. For example, smaller particle sizes with larger specific areas will improve the Li diffusion coefficient but trigger

more intensive side reactions with aqueous electrolytes, which will facilitate structural degradation and TM dissolution during cycling. In this case, more severe capacity decay and shorter cycle life can be observed among different cathode materials.

From the electrolyte perspective, a water-rich environment would reduce the crystallinity of cathode materials, facilitate TM dissolution and structural collapse, and finally lead to rapid cell failures. In comparison, with limited water content, the WIS and MC electrolytes alleviate the TM dissolution and inhibit bulk structure changes. Nevertheless, none of these electrolytes provides enough battery performance that can compete with conventional non-aqueous electrolytes. More extensive studies are needed to facilitate the development of aqueous batteries for practical applications, especially with focuses on the tradeoff between performance, cost of manufacturing, and safety.

#### Acknowledgments

The aqueous battery study was supported by the Naval Enterprise Partnership Teaming with Universities for National Excellence (NEPTUNE), Office of Naval Research (Grant #N000142312609) and the Program Manager, Corey T. Love. The synchrotron methods used to perform the characterization work were supported by and developed under the National Science Foundation (No. DMR-2045570). This research used resources of the Advanced Photon Source, a U.S. Department of Energy (DOE) Office of Science User Facility operated for the DOE Office of Science by Argonne National Laboratory under Contract no. DE-AC02-06CH11357. This research used 28-ID-1 beamline of the National Synchrotron Light Source II, a U.S. Department of Energy (DOE) Office of Science User Facility operated for the DOE Office of Science by Brookhaven National Laboratory under Contract No. DE-SC0012704.

#### **Author Contribution**

F.L. conceived and led the project. Y.Z. and F.L. designed experiments. Y.Z. performed materials preparation, characterization, and electrochemical experiments. D.H. and G.K. performed synchrotron XRD. A.H. and D. X. performed lab XRD and SEM. Y.Z., A.H. and L.L. performed XFM. Y.Z. and F.L. wrote the manuscript. All the authors have approved the final manuscript.

#### **ORCID**

Yuxin Zhang https://orcid.org/0000-0002-2830-4159 Dawei Xia https://orcid.org/0000-0003-4265-2528 Feng Lin https://orcid.org/0000-0002-3729-3148

#### References

- 1. B. Scrosati and J. Garche, J. Power Sources, 195, 2419 (2010).
- Y. Preger, H. M. Barkholtz, A. Fresquez, D. L. Campbell, B. W. Juba, J. Romàn-Kustas, S. R. Ferreira, and B. Chalamala, J. Electrochem. Soc., 167, 120532 (2020).
- 3. B. Dunn, H. Kamath, and J.-M. Tarascon, Science, 334, 928 (2011).
- N. Alias and A. A. Mohamad, *J. Power Sources*, 274, 237 (2015).
   D. Chao, W. Zhou, F. Xie, C. Ye, H. Li, M. Jaroniec, and S.-Z. Qiao, *Sci. Adv.*, 6, eaba4098 (2020).
- 6. C. Yang, J. Chen, X. Ji, T. P. Pollard, X. Lü, C.-J. Sun, S. Hou, Q. Liu, C. Liu, and T. Qing, Nature, 569, 245 (2019).
- 7. L. Suo, O. Borodin, W. Sun, X. Fan, C. Yang, F. Wang, T. Gao, Z. Ma, M. Schroeder, and A. von Cresce, Angew. Chem. Int. Ed., 55, 7136 (2016).
- 8. Y. Liang and Y. Yao, Nat. Rev. Mater, 8, 109 (2023).
- 9. W. Li, J. R. Dahn, and D. S. Wainwright, Science, 264, 1115 (1994).
- 10. L. Suo, O. Borodin, T. Gao, M. Olguin, J. Ho, X. Fan, C. Luo, C. Wang, and K. Xu, Science, 350, 938 (2015).
- 11. J. Zhang, C. Cui, P.-F. Wang, Q. Li, L. Chen, F. Han, T. Jin, S. Liu, H. Choudhary, and S. R. Raghavan, Energy Environ. Sci., 13, 2878 (2020).

  12. Y. Shen, B. Liu, X. Liu, J. Liu, J. Ding, C. Zhong, and W. Hu, Energy Storage
- Mater., 34, 461 (2021). 13. N. Dubouis, P. Lemaire, B. Mirvaux, E. Salager, M. Deschamps, and A. Grimaud,
- Energy Environ. Sci., 11, 3491 (2018).
- 14. L. Suo, D. Oh, Y. Lin, Z. Zhuo, O. Borodin, T. Gao, F. Wang, A. Kushima, Z. Wang, and H.-C. Kim, J. Am. Chem. Soc., 139, 18670 (2017).
- 15. J. Lim, K. Park, H. Lee, J. Kim, K. Kwak, and M. Cho, J. Am. Chem. Soc., 140, 15661 (2018).

- M. Turgeman, V. Wineman-Fisher, F. Malchik, A. Saha, G. Bergman, B. Gavriel, T. R. Penki, A. Nimkar, V. Baranauskaite, and H. Aviv, *Cell. Rep. Phys. Sci.*, 3, 100688 (2022).
- J. Zheng, G. Tan, P. Shan, T. Liu, J. Hu, Y. Feng, L. Yang, M. Zhang, Z. Chen, and Y. Lin, *Chem.* 4, 2872 (2018).
- 18. J. Xie, Z. Liang, and Y.-C. Lu, Nat. Mater., 19, 1006 (2020).
- 19. J. Xie, Y. Guan, Y. Huang, and Y.-C. Lu, Chem. Mater., 34, 5176 (2022).
- 20. D. Dong, J. Xie, Z. Liang, and Y.-C. Lu, ACS Energy Lett., 7, 123 (2021).
- C. Kuai, Z. Xu, C. Xi, A. Hu, Z. Yang, Y. Zhang, C.-J. Sun, L. Li, D. Sokaras, and C. Dong, *Nat. Catal.*, 3, 743 (2020).
- L. Mu, Z. Yang, L. Tao, C. K. Waters, Z. Xu, L. Li, S. Sainio, Y. Du, H. L. Xin, and D. Nordlund, J. Mater. Chem. A Mater., 8, 17487 (2020).
- M. M. Rahman, J. Mao, W. H. Kan, C.-J. Sun, L. Li, Y. Zhang, M. Avdeev, X.-W. Du, and F. Lin, ACS Mater. Lett., 1, 573 (2019).
- Y. Zhang, A. Hu, D. Xia, S. Hwang, S. Sainio, D. Nordlund, F. M. Michel, R. B. Moore, L. Li, and F. Lin, *Nat. Nanotechnol.*, 18, 790 (2023).
- T. Schwieters, M. Evertz, A. Fengler, M. Börner, T. Dagger, Y. Stenzel, P. Harte, M. Winter, and S. Nowak, J. Power Sources, 380, 194 (2018).

- B. Zhao, J. Li, M. Guillaume, J. Dendooven, and C. Detavernier, *Journal of Energy Chemistry*, 66, 295 (2022).
- Y. Shang, N. Chen, Y. Li, S. Chen, J. Lai, Y. Huang, W. Qu, F. Wu, and R. Chen, *Adv. Mater.*, 32, 2004017 (2020).
- 28. D. J. Morgan and S. Uthayasekaran, Surf. Interface Anal., 55, 556 (2023).
- 29. J. S. Forsythe and D. J. T. Hill, *Prog. Polym. Sci.*, 25, 101 (2000).
- 30. B. J. Lyons, Radiat. Phys. Chem., 45, 159 (1995).
- C. G. Torres-Castanedo, G. Evmenenko, N. S. Luu, P. M. Das, W. J. Hyun, K.-Y. Park, V. P. Dravid, M. C. Hersam, and M. J. Bedzyk, ACS Appl. Mater. Interfaces, 15, 35664 (2023).
- D. Tang, Y. Sun, Z. Yang, L. Ben, L. Gu, and X. Huang, *Chem. Mater.*, 26, 3535 (2014).
- 33. H. Yaghoobnejad Asl and A. Manthiram, *J. Am. Chem. Soc.*, **142**, 21122 (2020).
- Y. Zhang, A. Hu, E. Maxey, L. Li, and F. Lin, J. Electrochem. Soc., 169, 100512 (2022).
- M. Wood, J. Li, R. E. Ruther, Z. Du, E. C. Self, H. M. Meyer III, C. Daniel, I. Belharouak, and D. L. Wood III, *Energy Storage Mater.*, 24, 188 (2020).